Original Paper

Effects of natural fractures in cap rock on CO_2 geological storage: Sanduo Formation and Dainan Formation of the early Eocene epoch in the Gaoyou Sag of the Subei Basin

Yun-Zhao Zhang [a,b,*], Quan-Qi Dai [c,d,e,**], Lian-Bo Zeng [f], Rui-Qi Li [g], Rong-Jun Zhang [h,i], Le Qu [h,i], Yang-Wen Zhu [c,d,e], Hai-Ying Liao [c,d,e], Hao Wu [j]

a *710065*
b *710065*

c *102206*
d *102206*
e *y* *102206*
f *1022 9*
g *710018*
h *710065*
i *T* *710065*
j *y* *y* *730000*

ARTICLE INFO

Received 27 March 2024
Received in revised form
19 March 2025
Accepted 2 August 2025
Available online 7 August 2025

Edited by Xi Zhang and Jie Hao

Cap rock
Natural fractures
CO_2 geological storage

ABSTRACT

During the CO_2 injection and geological storage process, the integrity of the cap rock significantly influences the long-term safety of CO_2 storage. Natural fractures within the cap rock serve as potential pathways for CO_2 migration, thereby increasing the risk of CO_2 leakage. In this study, we determined the types, developmental characteristics, permeability changes, and CO_2-H_2O-Rock reactions of natural fractures in the mudstone cap rocks of the Sanduo Formation (E_3s) and Dainan Formation (E_2d) in the Gaoyou Sag of the Subei Basin using core observations, thin-section analysis, rock mechanics experiments, and paleomagnetic directional analysis. We identified four tectonic fracture sets (NNW, NWW, EW, and NE); high-angle shear fractures, ranging from 60° to 90° (average 82°) and typically measuring 4–12 cm (average 7.5 cm), dominate the assemblage, while slip fractures, ranging from 32° to 50° (average 36°) and measuring 3–6 cm (average 3.9 cm), are also present. At the microscale, shear fractures average 160 μm, and bedding fractures average 82 μm. Notably, 85.78% of shear fractures are unfilled, with calcite filling observed in 14.22%, while other fracture types show no filling. Permeability tests on samples without fractures reveal that permeability declines rapidly below 9 MPa, especially in shallower samples, followed by a slower reduction between 9 and 13 MPa, and ultimately stabilizes at approximately 0.00003 mD. In contrast, samples with fractures exhibit permeability that is 3–4 orders of magnitude higher; their fracture permeability decays according to a power law with pressure yet remains above 10 mD even at 46 MPa. Fractures with larger dip angles and those aligned with the maximum principal stress demonstrate the highest permeability. While silicate-filled fractures exhibit negligible changes in permeability, carbonate-filled fractures experience a temporary enhancement due to dissolution; however, subsequent permeability

disasters (Dar et al., 2022; Sennaoui et al., 2025). Currently, approximately 140 government organizations worldwide have committed to achieving net-zero carbon emissions, and the vision of carbon neutrality has become a global consensus (Ishaq and Crawford, 2023; Li et al., 2023b). The carbon emissions from the combustion of fossil fuels account for 33%–40% of the total global carbon emissions generated by human activities (Khatri et al., 2006; Liu et al., 2024). Due to the increasing global population and the accelerated industrialization process, there remains a strong dependence on fossil energy on a global scale for an extended period, and the demand for energy is expected to continue to rise (Sakthivel et al., 2024; Xu et al., 2023). Amidst the prominent contradiction between human development needs and climate and environmental concerns, Carbon Capture, Utilization, and Storage (CCUS) technology has become a more favorable option for achieving decarbonization goals due to its low implementation risks and uncertainties (Liu et al., 2023; Zhao et al., 2025). CO_2 storage is a crucial component of CCUS, and geological storage sites include depleted oil and gas reservoirs, unmineable coal seams, deep-sea locations, and deep saline aquifers (Chen et al., 2022; Li et al., 2023a; Yekeen et al., 2020). In particular, depleted oil and gas reservoirs serve as natural storage sites for CO_2. They possess well-contained systems and substantial storage capacity, ensuring high safety in the medium to long term. Additionally, by enhancing oil and gas recovery rates, operators can gain additional economic returns. Thus, depleted oil and gas reservoirs are considered ideal and economically viable locations for CO_2 geological storage (Bao et al., 2023; Wang et al., 2017). However, there is always a risk of leakage associated with the storage of CO_2 in depleted oil and gas reservoirs, as well as other geological storage methods (Bachu, 2016; Yang et al., 2023). If there is a large-scale, short-term leakage of stored CO_2, it could potentially lead to more severe natural disasters (Bachu and Adams, 2003; Hou et al., 2022). A low-permeability cap rock above the CO_2 reservoir is essential for effective CO_2 containment

887.0 0 7.9701 62.4755 365.4 0.86 0.4 0.17 0.01 k 1 j 1 J 0.000001 w 8.2887 k 1 j 1 J1 274.394 3 cm BT /F

and discussed the factors influencing the permeability of cap rock fractures after CO_2 injection and their impact on CO_2 geological storage.

2. Geological settings

2 1

Subei Basin is a Cenozoic rift basin formed above the Cretaceous basement. It is the onshore part of the Northern Jiangsu-South Yellow Sea Basin, with an area of approximately 35,000 km^2 (Fig. 1(a) and (b)) (Quaye et al., 2019). The basin trends northeastward, bounded by the Tan-Lu Fault to the west, connected to the SuLu Orogenic Belt to the north, extending eastward into the Yellow Sea, and delimited to the south by the Yangzhou-Rugao. After the early extensional faulting stage, late subsidence stage, and sagging stage, the basin formed successively from north to south, including the Yanfu Depression, Jianhu Uplift, and Dongtai Depression (Liu et al., 2016). The Gaoyou Sag is located in the southern part of the Subei Basin, generally trending northeast (Fig. 1(c)). It has a width of approximately 25–35 km from north to south, a length of about 100 km from east to west, and covers an area of approximately 2670 km^2. The southern part of the sag is adjacent to the Tongyang Uplift and Wubu Low Uplift, while the northern part is connected to the Zheduo Low Uplift by a gentle slope. In the west, it is connected to the Jinhu Sag through a saddle between the Liubu Low Uplift and the Lingtangqiao Low Uplift. To the east, it is bordered by the Baiju Depression. Formed during the Late Cretaceous Yezheng Movement and the Cenozoic Wubu Movement, the depression exhibits a characteristic funnel shape with a steep southern slope and a gentle northern slope (Zhu et al., 2023b). From south to north, the sag can be further divided into the southern steep slope zone, the central deep sag zone, and the northern slope zone (Fig. 1(d)).

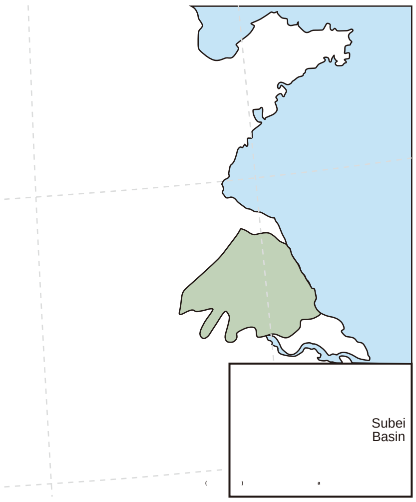

Fig. 1. (**a**–**b**) Geographical location of the Subei Basin in China. (**c**) Distribution of the main tectonic units in the Subei Basin. (**d**) Tectonic outline map of the Gaoyou Sag. Modified from Su et al., (2022).

2 2

The Cenozoic stratigraphy of the Gaoyou Sag, from the youngest to the oldest, comprises the Quaternary Dongtai Formation, the Neogene Yancheng Formation, the Eocene Sanduo Formation (E_3s), the Eocene Dainan Formation (E_2d), and the Paleogene Funing Formation (E_1f) (Fig. 2). Among these formations, the first (E_1f_1), second (E_1f_2), and third (E_1f_3) segments of the four-part Funing Formation serve as reservoirs, while the fourth segment (E_1f_4) functions as a hydrocarbon source rock (Quaye et al., 2022).

The Dainan Formation comprises Dainan Member 1 and Dainan Member 2, with thicknesses ranging from 200 to 950 m and 100–900 m, respectively. The primary lithologies include fine sandstone, sandstone, sandy mudstone, and mudstone. On the other hand, the Sanduo Formation consists of Sanduo Member 1 (E_2s_1) and Sanduo Member 2 (E_2s_2), with thicknesses ranging from 100 to 800 m and 50–800 m, respectively (Fig. 2). Its main lithologies include mudstone, muddy sandstone, fine sandstone, and sandy conglomerate. The Dainan Formation primarily represents fluvial, lacustrine, and swamp facies, while the Sanduo Formation reflects deposition in a hilly–fluvial plain terrain, characterized by river floodplains and interfluve basins (Zhu et al., 2023a). During the sedimentation period from E_2d to E_2s_1, two lake transgressions occurred, specifically during the sedimentation period of Dainan Member 1 Sub-member 1 ($E_2d_1^1$) and Sanduo Member 1 Sub-member 6 ($E_2s_1^6$). These events resulted in the formation of shore-shallow lake and semi-deep lake subfacies mudstones, constituting the primary regional cap rocks in the shallow formations of the Gaoyou Sag.

2 3

2 3 1

In the Gaoyou Sag, $E_2d_1^1$ comprises five sets of high-conductivity dark mudstones, featuring mud content ranging from 43% to 92%. The western single-layer mudstone exhibits greater thickness, reaching a maximum of around 100 m, while the eastern single-layer mudstone has a maximum thickness of less than 40 m (Fig. 3(a)). Overall, it shows a distribution pattern with thicker layers in the west and thinner layers in the east on the plane. In the Sag, $E_2s_1^6$ comprises one set of b4yBfi41B4MN9ABcmp8Tpkp0’i nk((0?%/zB1A)) than 1 MPa, exceeding 2 MPa in the deep sag zone, with the maximum reaching up to 10 MPa in the central part of the deep Sag. For the $E_2s_1^6$ cap rock, the displacement pressure ranges from 0.5 to 4 MPa, surpassing 2 MPa in

$$Z_1 = - \quad \sin\theta + Z\cos\theta$$

Table 3
Summary of the research materials.

Sample type	No.	Sample size	Lithology	Depth, m	Fracture dip, °	Fracture length, cm
Samples without fractures	1	25mm × 50 mm	Mudstone	1907.3	/	/
	2	25mm × 50 mm	Mudstone	1910.6	/	/
	3	25mm × 50 mm	Mudstone	2000.5	/	/
Samples with fractures	4	25mm × 50 mm	Mudstone	1907.4	89	4.99
	5	25mm × 50 mm	Mudstone	1910.5	62	4.41
	6	25mm × 50 mm	Mudstone	2000.2	47	3.65

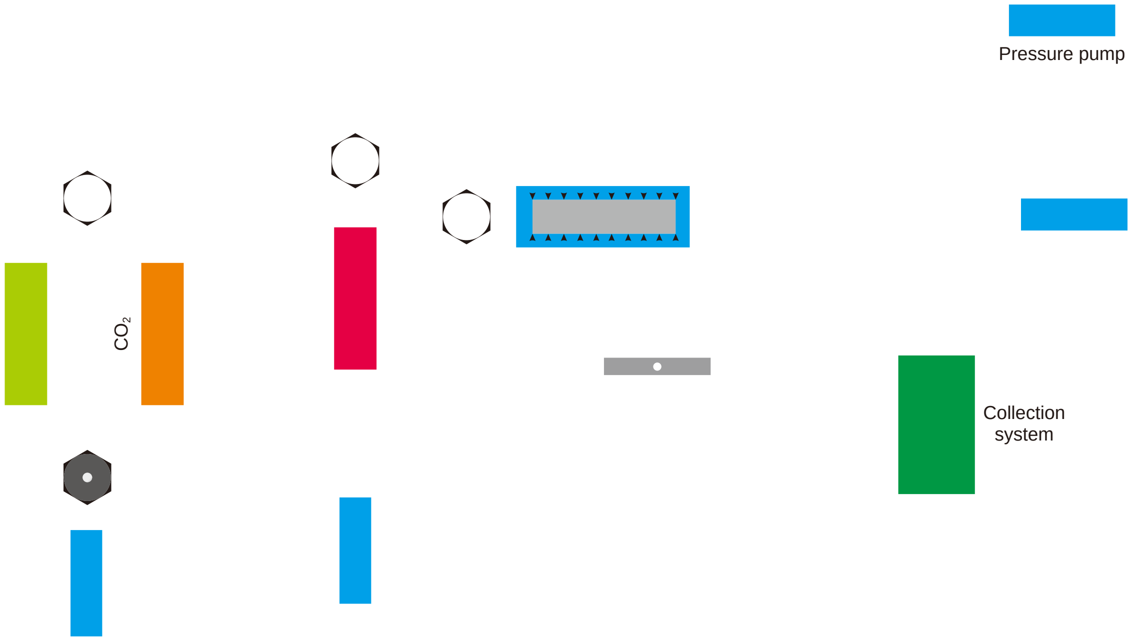

Fig. 6. Schematic diagram of the CO_2-H_2O-Rock reaction device.

dried in a drum, and then the length, diameter, and mass of the cores were measured (Table 4). Brine was prepared and added to the reactor, and the temperature and pressure were adjusted (Chen et al., 2023b). After sufficient reaction, the saturated carbonate solution was displaced, and the gas and water samples generated at different times were recorded. Samples from different reaction times were retrieved, and wet and dry samples were weighed. Mineral types and contents of samples at different reaction times were identified through EDS analysis.

4. Results

1

11 T

Based on the observation results from core and thin-section data, from the geological origin perspective of natural fractures, the cap rock natural fractures of the Paleogene Sanduo Formation and Dainan Formation in the Gaoyou Sag of the Subei Basin are classified into tectonic fractures and non-tectonic fractures (Figs. 7 and 8).

Tectonic fractures are the main type of natural fractures in the Paleogene Sanduo Formation and Dainan Formation cap rocks in the Gaoyou Sag of the Subei Basin. They are fractures formed under the influence of local tectonic events or tectonic stress fields. Tectonic fractures in the study area include tectonic shear fractures and tectonic slip fractures. Tectonic shear fractures have stable orientations, with straight and smooth surfaces, often showing slickenlines or even stepovers, and sometimes exhibiting calcite mineral fillings (Figs. 7(a), (d), and 8(a)). Tectonic slip fractures are a specific type of low-angle shear fractures that form when shear occurs along weak mudstone layers under tectonic compression or extension. Consequently, the angles between slip fractures and the maximum principal compressive stress (σ_1) do not conform to the shear angle distribution typically described by rock shear fracture criteria (Zeng et al., 2007). These fractures have smooth surfaces, sometimes displaying mirror-like features, with lower dip angles and shorter extension lengths (Fig. 7(b)).

Non-tectonic fractures are mainly composed of diagenetic fractures. Diagenetic fractures result from volume reduction during rock diagenesis, driven by geological processes such as compaction and pressure solution. In the study area, these

Table 4
Summary of the mudstone sample.

No.	Depth, m	Mass, g	Length, cm	Diameter, cm	Quartz, %	Potash feldspar, %	Plagioclase, %	Calcite, %	Chlorite, %	Illite, %
7	1915.7	39.57	3.72	2.50	34.2	4.2	21.3	13.7	1.7	24.9

fractures predominantly manifest as bedding fractures and dissolution fractures. Bedding fractures typically align parallel to the bedding planes, featuring small dip angles and exhibiting characteristics like bending, discontinuity, branching, and termination (Fig. 8(b)). However, they often demonstrate poor continuity. Dissolution fractures originate from differential dissolution processes. They may initially form as fractures and subsequently evolve into bead-like

1 2

The results of cap rock fracture orientations determined by core magnetic orientation indicate the presence of four sets of tectonic fractures in the study area, oriented NNW-SSE, NWW-SEE, nearly E-W, and NE-SW (Fig. 9). Among them, NE-oriented tectonic fractures have the highest proportion, followed by NNW-oriented fractures, while nearly E-W and NWW-oriented tectonic fractures have the lowest proportion.

Based on the inclination angle of tectonic fractures, they are classified into nearly vertical fractures (>80°), high-angle fractures (60–80°), intermediate-angle fractures (30–60°), low-angle fractures (10–30°), and nearly horizontal fractures (<10°). The statistical results of fracture dip angles from the core data show that the dip angles of tectonic shear fractures in the study area range between 60° and 90°, predominantly high-angle fractures, with an average dip angle of approximately 82° (Fig. 10). The dip angles of tectonic slip fractures range from 32° to 50°, mainly intermediate-angle fractures, with an average dip angle of around 36° (Fig. 10). Although we did not observe bedding fractures in the core, the dip angles of bedding fractures are expected to be in the range of 0–10°, mainly nearly horizontal fractures.

1 3

The statistical results from core drilling indicate that the lengths of tectonic shear fractures in the cap rock of the study area are typically less than 20 cm, mainly distributed in the range of 4–12 cm, with an average fracture length of approximately 7.5 cm (Fig. 11). The scale of tectonic slip fractures is usually less than 10 cm, distributed in the range of 3–6 cm, with an average fracture length of about 3.9 cm (Fig. 11). Thin-section observations show that the lengths of microscopic tectonic fractures range from 100 to 275 μm, with an average length of 160 μm. At the microscopic scale, the lengths of bedding fractures range from 50 to 120 μm, with an average length of 82 μm. Therefore, the lengths of tectonic fractures are greater than those of bedding fractures.

1

Based on the observation results of core samples in the study area, the linear density of tectonic shear fractures is 0.03 m^{-1}, the linear density of tectonic slip fractures is 0.07 m^{-1}, and the linear density of dissolution fractures is 0.01 m^{-1}. The results indicate differences in linear density among different types of fractures, reflecting variations in the development of different types of fractures.

Fig. 9. Rose diagram of cap rock fracture orientations determined by core magnetic orientation (= 12).

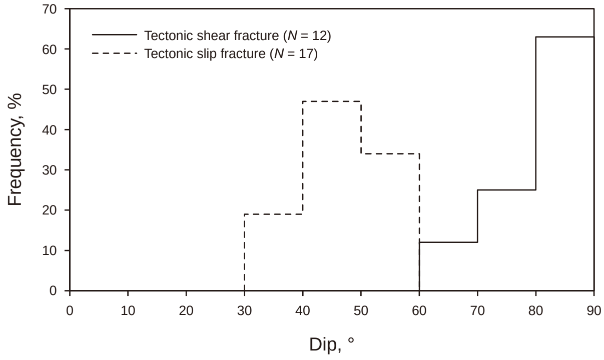

Fig. 10. Histogram of the frequency distribution of cap rock fracture dip angles.

1 5

The evaluation of fracture effectiveness includes the filling characteristics and aperture of the fractures. Based on measurements and observations of core fractures, the effectiveness characteristics of different types of fractures in the cap rock of the study area were determined. The statistical results show that unfilled fractures dominate in tectonic shear fractures, accounting for approximately 85.78%, while fully filled fractures constitute 14.22%, and partially filled fractures were not observed (Fig. 12). The filling material in these fractures is predominantly calcite (Fig. 7(d)). Tectonic slip fractures, bedding fractures, and dissolution fractures are all unfilled, with no observed filling material. The maximum aperture of dissolution fractures is up to 5 mm, with an average of approximately 1.49 mm. The aperture of unfilled tectonic shear fractures, slip fractures, and bedding fractures is generally <100 μm, with an average aperture of approximately 17.29 μm for tectonic shear fractures, 9.45 μm for slip fractures, and the smallest aperture for bedding fractures, averaging about 4.38 μm.

2 T

During the CO_2 injection process, as the pressure increases, fractures in the cap rock open when the pressure surpasses the opening pressure of natural fractures. In this study, the opening pressure of some natural fractures in the cap rock was calculated

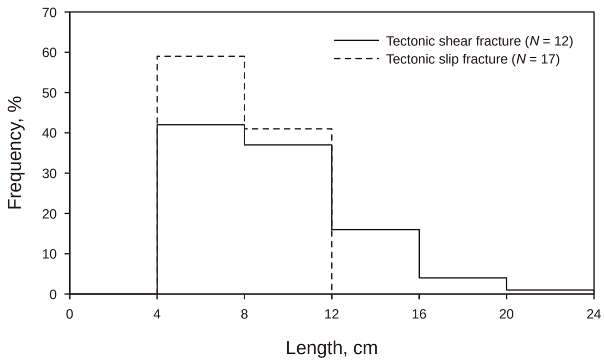

Fig. 11. Histogram of the frequency distribution of cap rock fracture lengths.

as an example. The calculation formula is as follows (Zeng et al., 2008):

$$\begin{aligned} &= \left(\frac{\mu}{1-\mu}\quad \rho_{s}\quad \sin\theta + \quad \rho_{s}\quad \cos\theta - \alpha\quad \rho_{w}\quad \right) \times 10^{-6} \\ &\quad \pm \quad \sigma_{1} \sin\beta\cos\beta \pm \quad \sigma_{3} \sin\beta\cos\beta \end{aligned}$$

in the equation, represents the static closure pressure of natural fractures, MPa; μ is the Poisson's ratio of the rock, dimensionless; α is the formation pressure coefficient, dimensionless; is the burial depth of the fracture, m; θ is the dip angle of the fracture, °; ρ_s is the rock density, kg/m^3; ρ_w is the density of water, kg/m^3; g is the gravitational acceleration, N/kg; β is the angle between the current horizontal maximum principal stress and the fracture trend, °; σ_1 and σ_3 are the gradients of the horizontal maximum and minimum principal stresses, with positive values indicating compressive stress and negative values indicating tensile stress, MPa/m. The Poisson's ratio (μ) is determined through rock mechanics experiments. The study area exhibits normal formation pressure, with the pressure coefficient ranging from 0.8 to 1.0; α is considered as the average value, 0.9; ρ_s, ρ_w, , and θ are all based on measured data; the current direction of the maximum horizontal principal stress is approximately E-W, and the fracture trend is determined by core magnetic orientation to obtain β; the current maximum principal stress gradient is approximately −0.01509 MPa/m, and the minimum principal stress gradient is 0.0196 MPa/m (Chen, 2009). The calculation results are shown in Table 5.

3 *T*

The experimental results of overburden gas permeability for samples without fractures show that, with increasing confining pressure, the matrix permeability of samples at different burial depths gradually decreases (Fig. 13). When the confining pressure is less than 9 MPa, the matrix permeability declines rapidly, with shallower samples exhibiting a significantly greater reduction compared to the sample at a burial depth of 2000.5 m. As the confining pressure increases to between 9 and 13 MPa, the rate of permeability reduction gradually slows down. With a further increase in confining pressure beyond 13 MPa, the matrix permeability of samples at different burial depths becomes nearly identical, decreasing to approximately 0.00015 mD. [illegible]

Potassium feldspar, mainly composed of $KAlSi_3O_8$, saw its content rise from 4.2% to 10.7% (Fig. 15). Plagioclase, composed primarily of $NaAlSi_3O_8$, experienced an increase in content from 21.3% to 31.7% (Fig. 15). Calcite, mainly consisting of $CaCO_3$, initially decreased in content from 10.7% to 1.4%, then increased to 7%, before decreasing to 0 (Fig. 15). Clay minerals, primarily composed of kaolinite, illite, and montmorillonite, decreased overall from 29.6% to 20.5% (Fig. 15). Dolomite, composed mainly of $CaMg(CO_3)_2$, increased from 0 to 8.2%, then decreased back to 0 (Fig. 15).

5. Discussion

5 1

2

5 1 1

(1) Fracture burial depth

Due to the influence of the current stress field, fractures with different orientations at the same depth experience varying opening pressures. Therefore, when studying the impact of fracture burial depth on the opening pressure, it is necessary to focus on fractures with the same orientation. Under the same orientation conditions (fracture dip angle $(\theta) = 68.3^\circ$, fracture dip angle between the current horizontal maximum principal stress and the fracture trend $(\beta) = 33.8^\circ$), the relationship between burial depth (H) and opening pressure ( ) indicates that for fractures with the same orientation and dip angle, the deeper the burial position, the greater the opening pressure, making inB79MN9AfiBTnp J(1)W BT@pq959tween

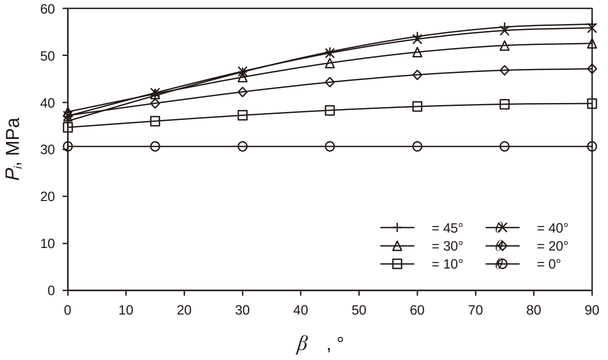

Fig. 18. Relationship between the angle between the current maximum horizontal principal stress direction and the fracture trend and the opening pressure of fractures ($\theta = 0$–$45°$). is the average value taken from 4 samples, 1963.7 m; μ is the average value taken from 4 samples, 0.36; ρ is the average value taken from 4 samples, 2510 kg/m^3.

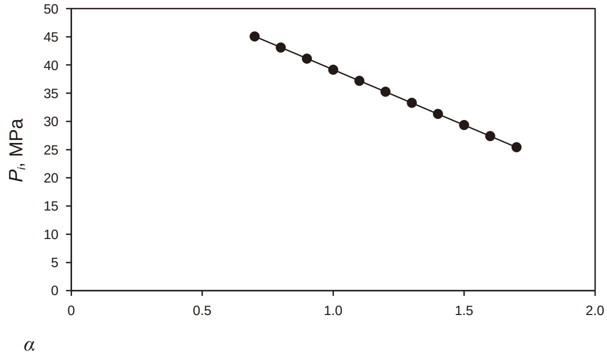

Fig. 19. Relationship between the coefficient of formation pressure and the opening pressure of fractures at $\theta = 68.3°$, $\beta = 33.8°$, $= 1963.7$ m. μ is the average value taken from 4 samples, 0.36; ρ_s is the average value taken from 4 samples, 2510 kg/m^3.

smaller opening pressures, making them more prone to opening (Figs. 17 and 18). The influence of the current stress field on the opening pressure of fractures is mainly manifested when, under constant conditions, the smaller the angle between the direction of the maximum principal stress and the trend of the fracture, the smaller the opening pressure of the fracture. Conversely, the larger the angle, the greater the opening pressure of the fracture. As the orientation of fractures changes, the static rock confining pressure experienced by the fracture surfaces varies, leading to different pressures required for the fractures to reopen. Fractures nearly parallel to the direction of the maximum principal stress ($\beta = 0°$) are in a tensile state with a large underground opening, resulting in the minimum opening pressure. Fractures nearly perpendicular to the direction of the maximum principal stress ($\beta = 90°$) are in a compressive state with a small underground opening, resulting in the maximum opening pressure. Fractures obliquely intersecting with the direction of the maximum principal stress exhibit a combined tensile and shear state with an underground opening between the aforementioned two cases, resulting in an opening pressure between the two extremes. It is worth noting that when the dip angle of fractures is distributed between 0° and 10°, the angle between the current stress field direction and the trend of the fracture has almost no effect on the opening pressure of the fracture. At this point, the opening pressure of the fracture is only influenced by the overlying formation pressure. Based on the development characteristics of natural fractures in the study area, the opening pressure of fractures with different orientations, arranged from smallest to largest, is approximately as follows: nearly E-W, NWW-SEE, NE-SW, and NNW-SSE directions.

(3) Pore fluid pressure

The relationship between the formation pressure coefficient and the opening pressure of fractures indicates that, within the same depth range, fractures with the same orientation in an abnormally high-pressure fluid environment have smaller opening pressures compared to fractures in a static hydrostatic pressure environment (Fig. 19). Fractures in an abnormally high-pressure environment are more easily opened because the fluid bears a greater load, reducing the confining pressure effect on the fractures, i.e., decreasing the opening pressure of the fractures. Conversely, when the pore fluid pressure is less than static hydrostatic pressure, the skeleton bears more force, leading to an increase in the opening pressure of the fractures. Therefore, cap rocks in low-pressure or ambient-pressure environments are less prone to fracture opening compared to those in high-pressure environments, exhibiting better CO_2 storage capacity.

5 1 2 T 2

With the increasing injection of CO_2, the formation pressure gradually rises, causing instability in the formation. The range affected by pressure increments in the cap rock continues to expand (Qin et al., 2022). If the pressure within the cap rock becomes too high, it not only leads to the formation of new fractures but also results in the further opening, extension, and expansion of existing natural fractures in the cap rock, leading to the failure of CO_2 storage (Lavrov, 2016). Due to the generally lower opening pressure of existing natural fractures, especially high-angle tectonic fractures, compared to the formation fracturing pressure, the injection pressure may cause fractures to open and extend before inducing formation fracturing (Zeng et al., 2023). In this scenario, determining reasonable CO_2 injection pressure limits should not rely on the formation fracturing pressure but rather on the opening pressure of fractures to avoid widespread fracture opening and CO_2 leakage. For CO_2 geological storage, critical input parameters such as the shallowest burial depth of the cap rock, the maximum value of the formation pressure coefficient, the maximum dip angle of fractures, and the minimum angle between the current maximum principal stress direction and fracture trend should be chosen. This approach will help control internal pressure within the cap rock, prevent further opening and extension of cap rock fractures, and effectively enhance the overall CO_2 storage capacity.

5 2

2

5 2 1

(1) Fracture orientation and current maximum principal stress

Under the influence of overlying lithostatic pressure, the normal stress acting on the low-angle fracture surface is significantly greater than that on the high-angle fracture surface. This results in larger apertures for high-angle fractures compared to low-angle fractures, indicating better effectiveness. Therefore, as the dip angle of fractures increases, the permeability of fractures also increases. The relationship between the fracture trend and the direction of the current maximum principal stress is as follows: fractures parallel to the current maximum principal stress direction have larger apertures, better connectivity, higher permeability, and represent the main flow direction. In contrast, fractures perpendicular to the current maximum principal stress direction, due to the larger normal stress acting perpendicular to the fracture surface, tend to be closed and are less effective. Fractures with orientations oblique to the current maximum principal stress direction fall between the two categories, and as the angle between them increases, the aperture and permeability of fractures decrease (Zeng and Li, 2009). Therefore, fractures with larger dip angles and orientations consistent with the current stress direction exhibit the highest permeability.

(2) Effective stress

External effective stress is a crucial factor influencing the permeability of cap rock fractures, and fractures with different dip angles exhibit significant pressure sensitivity. Under the influence of overlying lithostatic pressure, the normal stress acting on the low-angle fracture surface is notably greater than that on the high-angle fracture surface. Consequently, high-angle fractures exhibit larger apertures than low-angle fractures, indicating a stronger permeability for high-angle fractures. Therefore, as the dip angle of fractures decreases and effective stress increases, the aperture of fractures decreases, leading to a reduction in the permeability of fractures. It is worth noting that, despite the decrease in aperture, experimental results on fracture permeability indicate that in the deep Jurassic tight sandstone reservoirs at the southern margin of the Junggar Basin, where fracture burial depth exceeds 8000 m (with confining and axial pressures reaching 115 MPa), the fracture permeability can still reach around 20 mD (Mao et al., 2020). The permeability of natural fractures remains over 400 times higher than the matrix permeability of the reservoir. Therefore, natural fractures continue to serve as essential storage spaces and main flow channels in deep tight reservoirs. It can be reasonably inferred that natural fractures in the cap rock may not completely close with increasing effective stress or burial depth. Natural fractures remain potential pathways for CO_2 leakage, posing an increased risk of CO_2 storage failure.

(3) Mineral composition of fractures and types of fillings

Based on the filling conditions of natural fractures, they can be classified as unfilled, partially filled, or fully filled (Zhang et al., 2021b). Unfilled fractures consist of the fracture walls and voids, partially filled fractures consist of the fracture walls, voids, and filling materials, while filled fractures consist of the fracture walls and filling materials. In the study area, cap rock fractures were found to be filled only with calcite, and other common types of natural fracture fillings include minerals like quartz, clay, and dolomite (Zeng et al., 2012). The fracture walls may be composed of carbonate or silicate minerals. Under the influence of carbonation, fracture walls or filling materials may undergo dissolution or form new mineral precipitates, leading to changes in fracture aperture or closure and alterations in fracture permeability (Laubach et al., 2019; Laubach, 2003). Therefore, it is essential to consider the mineral composition of fracture walls and the types of filling materials.

In acidic environments, most silicate minerals, including feldspar, mica, and clay minerals, exhibit high instability and are prone to dissolution in water (Fig. 15). Simultaneously, under suitable conditions, new minerals can form (Pham et al., 2011; Zhang et al., 2015). As the H^+ concentration increases, the dissolution rates of most silicate minerals rapidly increase exponentially, while the dissolution rate of quartz remains nearly constant or even slowly decreases (Dove and Crerar, 1990). Consequently, for unfilled fractures with quartz as the component of the fracture walls, there is minimal reaction with carbonic acid, resulting in little to no change in the aperture and permeability of the fractures. However, if the mineral composition of the fracture walls includes other silicate minerals, new mineral precipitates may form. For instance, minerals such as kaolinite, muscovite, alunite, and quartz could potentially obstruct the fracture pathways, reducing the permeability of the fractures (Rosenbauer et al., 2005; Watson et al., 2004). Similarly, if the filling material in the fractures is clay minerals, especially smectite, it may react with H_2CO_3 to form new minerals such as iron dolomite, quartz, and kaolinite (Kurnosov et al., 2020), resulting in minimal changes in the permeability of the fractures. Since quartz-filled fractures resist dissolution by H_2CO_3, the permeability of quartz-filled fractures remains almost unchanged. The increased amount of quartz primarily stems from the reaction between H_2CO_3 and smectite and feldspar. Most carbonate minerals, such as calcite, magnesite, siderite, and dolomite, are susceptible to reactions with carbonic acid (Fig. 15). For unfilled fractures with carbonate minerals as components of the fracture walls, they may react with carbonic acid and dissolve (Du et al., 2018; Yu et al., 2012), resulting in localized increases in fracture aperture. Similarly, if the filling material in the fractures comprises calcite and dolomite veins, the veins may gradually dissolve in H_2CO_3, creating localized high-permeability channels and significantly increasing the permeability of the fractures. It is worth noting that when CO_2 is injected into geological formations containing calcite-filled fractures, it can react with the groundwater and existing calcite minerals. This reaction may lead to the dissolution of calcite, releasing calcium and carbonate ions into the solution. Under certain conditions such as changes in pressure, temperature, or chemical composition of the solution, these calcium and carbonate ions may re-precipitate as carbonate minerals, such as calcite or dolomite, within the fractures. Therefore, early exposure to H_2O and CO_2 may result in an increase in the content of calcite and dolomite, but ultimately, they will be completely dissolved (Fig. 15).

5 2 2

2

After the injection of CO_2 into the reservoir, it migrates upward continuously under the influence of buoyancy and injection pressure, accumulating extensively beneath the cap rock. CO_2 infiltrates the cap rock by breaking through capillary forces between the reservoir and cap rock or using fractures between the reservoir and cap rock as pathways. Consequently, CO_2-H_2O-Rock reactions occur within the cap rock fractures. In the context of oil and gas reservoir exploration and development, filled fractures, having nearly lost their permeability, are considered ineffective. Partially filled and unfilled fractures, exhibiting permeability, are deemed effective. Initially, unfilled fractures in the cap rock have higher permeability. As the CO_2-H_2O-Rock reaction progresses, CO_2

encounters silicate minerals in the cap rock fracture pathways, resulting in either new precipitation or no reaction. This leads to a reduction or minimal change in the fractures' permeability to CO_2. In cap rock fractures where CO_2 encounters carbonate minerals, dissolution occurs, increasing the aperture of the fractures and enhancing the permeability to CO_2, consequently raising the risk of CO_2 leakage. Filled fractures in the cap rock initially have lower porosity and permeability, providing minimal conduits for CO_2 migration. As the CO_2-H_2O-Rock reaction continues, the permeability of fractures filled with quartz and clay remains essentially unchanged. The former experiences no CO_2-H_2O-Rock reaction, while the latter forms new mineral precipitates, promoting fracture closure. Fractures filled with calcite and dolomite witness an increase in permeability as the CO_2-H_2O-Rock reaction progresses. After the complete dissolution of the veins, the permeability of fractures is jointly controlled by effective stress, fracture orientation, and the current maximum principal stress. Therefore, changes in CO_2 permeability follow a similar trend to unfilled fractures. Regardless of whether it is carbonate minerals in fracture walls or fracture fillings, in the CO_2-H_2O-Rock system, besides the dissolution of carbonate cement in fractures, variations in CO_2 concentration, pressure, ambient temperature, hydrodynamic conditions, and calcium ion concentration can lead to the formation of carbonate cement (Xu et al., 2003; Zhu et al., 2011). Secondary precipitation processes can result in the plugging of fractures with calcite and dolomite, aiding in self-sealing of the fractures, which may potentially reduce their permeability. Thus, during the geological storage of carbon dioxide, changes in other conditions are also significant factors affecting the CO_2-H_2O-Rock reaction in cap rocks and the permeability of carbonate-filled fractures.

Overall, different types of fractures exhibit varying impacts on CO_2 geological storage. High-angle tectonic fractures and fractures oriented parallel to the current stress direction pose the highest risk of leakage in CO_2 geological storage. In comparison to high-angle tectonic fractures, laterally distributed bedding fractures dominate the lateral migration of CO_2. The intermittent and discontinuous distribution of these bedding fractures, coupled with the influence of overlying formation pressure, results in relatively poor aperture and permeability, thereby reducing the risk of CO_2 leakage into the cap rock. The impact of differently filled fractures on CO_2 geological storage is characterized by a higher risk of CO_2 leakage in fractures filled with carbonate minerals like calcite and dolomite due to prolonged CO_2-H_2O-Rock reactions. In contrast, fractures filled with silicate minerals such as quartz pose a lower risk of CO_2 leakage.

6. Conclusions

(1) In the Gaoyou Sag of the Subei Basin, mudstone cap rocks from the Paleogene Sanduo and Dainan Formations contain tectonic (shear and slip) and non-tectonic (bedding and dissolution) fractures. Tectonic fractures trend NNW-SSE, NWW-SEE, E-W, and NE-SW. Shear fractures are high-angle, slip fractures are moderate-angle, and bedding fractures are near-horizontal. Tectonic fractures are larger but less dense than diagenetic ones, with some fully filled by calcite.

(2) Natural fractures significantly increase CO_2 leakage risk. Fractured samples have permeability three to four orders of magnitude higher than intact samples. Fracture permeability decreases with pressure but remains above 10 mD even at 46 MPa.

(3) CO_2 injection pressure limits should be based on fracture opening pressure rather than cap rock fracturing pressure. Factors like burial depth, fracture dip, and alignment with the maximum principal stress should be considered to prevent further fracture opening and CO_2 leakage.

(4) Fracture permeability is controlled by orientation, stress, mineral composition, and filling material. High-angle fractures aligned with the stress direction have the highest permeability. Increased effective stress reduces permeability, while CO_2-H_2O-Rock interactions modify permeability based on mineral content.

(5) High-angle fractures aligned with the stress direction pose the greatest CO_2 leakage risk. Bedding fractures promote lateral CO_2 migration, reducing vertical leakage risk. [illegible]

References

Al-Yaseri, A., Yekeen, N., Ali, M., et al., 2022. Effect of organic acids on CO_2-rock and water-rock interfacial tension: implications for CO_2 geo-storage. J. Pet. Sci. Eng. 214, 110480. https://doi.org/10.1016/j.petrol.2022.110480.

Ali, M., Jha, N.K., Pal, N., et al., 2022. Recent advances in carbon dioxide geological storage, experimental procedures, influencing parameters, and future outlook. Earth Sci. Rev. 225, 103895. https://doi.org/10.1016/j.earscirev.2021.103895.

Antropov, A., Lavrov, A., Orlic, B., 2017. Effect of in-situ stress alterations on flow through faults and fractures in the cap rock. Energy Proc. 114, 3193–3201. https://doi.org/10.1016/j.egypro.2017.03.1449.

Asem, P., Gardoni, P., 2022. A probabilistic, empirical model for permeability of mudstone. Probab. Eng. Mech. 69, 103291. https://doi.org/10.1016/j.probengmech.2022.103262.

Bachu, S., 2016. Identification of oil reservoirs suitable for CO_2-EOR and CO_2 storage (CCUS) using reserves databases, with application to Alberta, Canada. Int. J. Greenh. Gas Control 44, 152–165. https://doi.org/10.1016/j.ijggc.2015.11.013.

Bachu, S., Adams, J.J., 2003. Sequestration of CO_2 in geological media in response to climate change: capacity of deep saline aquifers to sequester CO_2 in solution. Energy Convers. Manag. 44 (20), 3151–3175. https://doi.org/10.1016/S0196-8904(03)00101-8.

Bachu, S., Bonijoly, D., Bradshaw, J., et al., 2007. CO_2 storage capacity estimation: methodology and gaps. Int. J. Greenh. Gas Control 1 (4), 430–443. https://doi.org/10.1016/S1750-5836(07)00086-2.

Bachu, S., Shaw, J., 2003. Evaluation of the CO_2 sequestration capacity in Alberta's oil and gas reservoirs at depletion and the effect of underlying aquifers. J. Can. Pet. Technol. 42 (9), 51–61. https://doi.org/10.2118/03-09-02.

Bao, X.L., Fragoso, A., Aguilera, R., 2023. Simultaneous enhanced oil recovery, CCUS and UHUS in shale oil reservoirs. Int. J. Coal Geol. 275, 104306. https://doi.org/10.1016/j.coal.2023.104301.

Cao, D.S., Zeng, L.B., Gomez-Rivas, E., 2024. Correction of linear fracture density and error analysis using underground borehole data. J. Struct. Geol. 184, 105152. https://doi.org/10.1016/j.jsg.2024.105152.

Chen, B.W., Wang, R., Li, Q., et al., 2023a. Status and advances of research on caprock sealing properties of CO_2 geological storage. Geol. J. China Univ. 29 (1), 85–99. https://doi.org/10.16108/j.issn1006-7493.2023010 (in Chinese).

Chen, H., Yu, H.Z., Zhou, B., et al., 2023b. Storage mechanism and dynamic characteristics of CO_2 dissolution in saline aquifers. Energy Fuel. 37 (5), 3875–3885. https://doi.org/10.1021/acs.energyfuels.2c03987.

Chen, Q., 2009. Research on Structure Stress and Controlling on Structure in Western Gaoyou Depression of Subei Basin. PhD Thesis. China University of Petroleum (East China).

Chen, X.S., Li, Y.P., Jiang, Y.L., et al., 2022. Theoretical research on gas seepage in the formations surrounding bedded gas storage salt cavern. Pet. Sci. 19 (4), 1766–1778. https://doi.org/10.1016/j.petsci.2022.01.021.

Dar, A.A., Hameed, J., Huo, C., et al., 2022. Recent optimization and panelizing measures for green energy projects; insights into CO_2 emission influencing to circular economy. Fuel 314, 123094. https://doi.org/10.1016/j.fuel.2021.123094.

Dove, P.M., Crerar, D.A., 1990. Kinetics of quartz dissolution in electrolyte solutions using a hydrothermal mixed flow reactor. Geochem. Cosmochim. Acta 54 (4), 955–969. https://doi.org/10.1016/0016-7037(90)90431-J.

Du, Y., Sang, S.X., Wang, W.F., et al., 2018. Experimental study of the reactions of supercritical CO_2 and minerals in high-rank coal under formation conditions. Energy Fuel. 32 (2), 1115–1125. https://doi.org/10.1021/acs.energyfuels.7b02650.

Durham, W.B., Bourcier, W.L., Burton, E.A., 2001. Direct observation of reactive flow in a single

Li, Y., Wang, R., Zhao, Q.M., et al., 2023b. A CO_2 storage potential evaluation method for saline aquifers in a petroliferous basin. Petrol. Explor. Dev. 50 (2), 484–491. https://doi.org/10.1016/S1876-3804(23)60403-3.

Li, Z.W., Dong, M.Z., Li, S.L., et al., 2006. CO_2 sequestration in depleted oil and gas reservoirs—caprock characterization and storage capacity. Energy Convers. Manag. 47 (11–12), 1372–1382. https://doi.org/10.1016/j.enconman.2005.08.023.

Liu, C., Xie, Q.B., Wang, G.W., et al., 2016. Reservoir properties and controlling factors of contact metamorphic zones of the diabase in the northern slope of the Gaoyou Sag, Subei Basin, eastern China. J. Nat. Gas Sci. Eng. 35, 392–411. https://doi.org/10.1016/j.jngse.2016.08.070.

Liu, H.C., Lu, H., Hu, H., 2024. CO_2 capture and mineral storage: state of the art and future challenges. Renew. Sustain. Energy Rev. 189, 113908. https://doi.org/10.1016/j.rser.2023.113908.

Liu, Y., Chen, Q.H., Wang, X., et al., 2017. Influence of normal fault growth and linkage on the evolution of a rift basin: a case from the Gaoyou depression of the Subei Basin, eastern China. AAPG Bull. 101 (2), 265–288. https://doi.org/10.1306/06281615008.

Liu, Z.X., Gao, M., Zhang, X.M., et al., 2023. CCUS and CO_2 injection field application in abroad and China: Status and progress. Geoenergy Sci. Eng. 229, 212011. https://doi.org/10.1016/j.geoen.2023.212011.

Ma, C.F., Lin, C.Y., Dong, C.M., et al., 2020. Quantitative relationship between argillaceous caprock thickness and maximum sealed hydrocarbon column height. Nat. Resour. Res. 29 (3), 2033–2049. https://doi.org/10.1007/s11053-019-09554-w.

Mao, Z., Zeng, L.B., Liu, G.P., et al., 2020. Characterization and effectiveness of natural fractures in deep tight sandstones at the south margin of the Junggar Basin, northwestern China. Oil Gas Geol. 41 (6), 1212–1221. https://doi.org/10.11743/ogg20200609 (in Chinese).

Pham, V.T.H., Lu, P., Aagaard, P., et al., 2011. On the potential of CO_2-water-rock interactions for CO_2 storage using a modified kinetic model. Int. J. Greenh. Gas Control 5 (4), 1002–1015. https://doi.org/10.1016/j.ijggc.2010.12.002.

Qin, J., Zhong, Q.H., Tang, Y., et al., 2022. CO_2 storage potential assessment of offshore saline aquifers in China. Fuel 341, 127681. https://doi.org/10.1016/j.fuel.2023.127681.

Qiu, Y.F., 2022. Comprehensive evaluation of medium-shallow caprocks conditions in deep depression zone of Gaoyou Sag. Complex Hydrocarb. Reserv. 15 (1), 8–12 (in Chinese).

Quaye, J.A., Jiang, Z.X., Liu, C., et al., 2022. Biogenically modified reservoir rock quality: a case from the lowermost member Paleocene Funing Formation, Gaoyou Depression, Subei Basin, China. J. Pet. Sci. Eng. 219, 111126. https://doi.org/10.1016/j.petrol.2022.111126.

Quaye, J.A., Jiang, Z.X., Zhou, X.W., 2019. Bioturbation influence on reservoir rock quality: a case study of well Bian-5 from the second member Paleocene Funing Formation in the Jinhu Sag, Subei Basin, China. J. Pet. Sci. Eng. 172, 1165–1173. https://doi.org/10.1016/j.petrol.2018.09.026.

Rohmer, J., Pluymakers, A., Renard, F., 2016. Mechano-chemical interactions in sedimentary rocks in the context of CO_2 storage: Weak acid, weak effects? Earth Sci. Rev. 157, 86–110. https://doi.org/10.1016/j.earscirev.2016.03.009.

Rosenbauer, R.J., Koksalan, T., Palandri, J.L., 2005. Experimental investigation of CO_2-brine-rock interactions at elevated temperature and pressure: Implications for CO_2 sequestration in deep-saline aquifers. Fuel Process. Technol. 86 (14–15), 1581–1597. https://doi.org/10.1016/j.fuproc.2005.01.011.

Rui, Z.H., Zeng, L.B., Dindoruk, B., 2025. Challenges in the large-scale deployment of CCUS. Engineering 44, 17–20. https://doi.org/10.1016/j.eng.2024.11.031.

Rutqvist, J., Tsang, C.F., 2002. A study of caprock hydromechanical changes associated with CO_2-injection into a brine formation. Environ. Geol. 42 (2–3), 296–305. https://doi.org/10.1007/s00254-001-0499-2.

Sakthivel, S., Yekeen, N., Theravalappil, R., et al., 2024. Influence of carbon nanodots on the carbonate/CO_2/brine wettability and CO_2-brine interfacial tension: Implications for CO_2 geo-storage. Fuel 355, 129404. https://doi.org/10.1016/j.fuel.2023.129404.

Sennaoui, B., Ling, K., Ostadhassan, M., et al., 2025. Subsurface CO_2 storage in unconventional reservoirs: Insights into pore-scale characterization of geochemical interactions and particle migration. Geoenergy Sci. Eng. 247, 213688. https://doi.org/10.1016/j.geoen.2025.213688.

Smith, D.A., 1966. Theoretical considerations of sealing and non-sealing faults. AAPG Bull. 50 (2), 363–374. https://doi.org/10.1306/5D25B48F-16C1-11D7-8645000102C1865D.

Song, J., Zhang, D.X., 2013. Comprehensive review of caprock-sealing mechanisms for geologic carbon sequestration. Environ. Sci. Technol. 47 (1), 9–22. https://doi.org/10.1021/es301610p.

Su, A., Chen, H.H., Feng, Y.X., et al., 2022. Multistage fracturing history in the Paleocene lacustrine shale oil reservoirs of the Subei Basin, Eastern China. Mar. Petrol. Geol. 144, 105835. https://doi.org/10.1016/j.marpetgeo.2022.105835.

Tremosa, J., Mito, S., Audigane, P., et al., 2017. Experimental assessment of well integrity